Polymer 53 (2012) 3360–3367

Contents lists available at SciVerse ScienceDirect

Polymer

journal homepage: www.elsevier.com/locate/polymer

An in-situ simultaneous SAXS and WAXS survey of PEBAX® nanocomposites reinforced with organoclay and POSS during uniaxial deformation

Tahseen Kamal[a], Soo-Young Park[a,*], Myong-Chan Choi[b], Young-Wook Chang[b,c], Wei-Tsung Chuang[d], U-Ser Jeng[d]

[a] Department of Polymer Science, Kyungpook National University, #1370 Sangyuk-dong, Buk-gu, Daegu 702-701, South Korea
[b] Department of Bionano Technology, Hanyang University, Ansan 426-791, South Korea
[c] Department of Chemical Engineering, Hanyang University, Ansan 426-791, South Korea
[d] National Synchrotron Radiation Research Center, 101 Hsin-Ann Road, Hsinchu 30076, Taiwan

ARTICLE INFO

Article history:
Received 7 March 2012
Received in revised form
2 May 2012
Accepted 19 May 2012
Available online 26 May 2012

Keywords:
Poly(ether-b-amide)
Organoclay
Trisilinolphenyl-POSS

ABSTRACT

Poly(ether-block-amide) (PEBA), commercially known as PEBAX®, nanocomposites filled with organically modified clay (Cloisite 30B) and trisilinolphenyl-polyhedral oligomeric silsesquioxane (tsp-POSS) were prepared by a melt mixing method, respectively. The structures of the nanocomposites were investigated using differential scanning calorimetry (DSC), Fourier transform infrared (FT-IR) spectroscopy, and in-situ simultaneous small and wide angle X-ray scatterings (SAXS and WAXS) during uniaxial deformation. The FT-IR spectra showed the hydrogen bonding between the fillers and the PEBA which helped to disperse the fillers in the polymer matrix. The crystallinities and mechanical properties of the nanocomposites were improved compared to the neat polymer. Their origins were studied with an in-situ simultaneous SAXS and WAXS technique during the uniaxial deformation.

1. Introduction

A number of polymers have been explored by compositing them with different nano-sized fillers to enhance or bring about various properties. The semi-crystalline polymers are commonly chosen to enhance their mechanical properties in the composites. In order to tune their mechanical properties, the semi-crystalline polymers have sometimes been copolymerized (or blended) with amorphous polymers [1–3]. Among them, poly(ether-b-amide) is a class of thermoplastic elastomers in the form of a muliblock copolymer and its properties in the final product are controlled by varying the composition of polyether and polyamide segments during its synthesis [1–3]. Atochem© developed high molecular weight poly(ether-b-amide) in 1980 by using the tetra-alkoxide catalyst family under the trade name of PEBAX® in which poly(tetramethylene ether) glycol (PTMO) and polyamide-12 (PA-12) were used as the soft and hard segments, respectively. Various grades of PEBA have been synthesized by varying the amide and ether composition for applications in a wide variety of products, such as virus-proof surgical equipments, food packaging materials, antistatic sheets or belts, films for textile lamination used in sportswears and gloves, etc [4]. The nano-sized fillers were incorporated into PEBA to improve or meet some required properties for certain purposes [5]. For example, organically modified clay and trisilinolphenyl-polyhedral oligomeric silsesquioxane (tsp-POSS) were used to improve the properties in gas separating and filtering membranes and fire-proof polymer products [6–8]. However, the origin of the improved properties has not been fully explored. The well-dispersed nano-scale fillers in the polymer matrix provide large interfacial region, which can control the overall physical properties. The large interfacial area also influences the crystal structure in the crystalline composite matrix which in turn correlates their mechanical properties. In the case of elastomers, large tensile deformation is possible, therefore, the investigation of structural changes during drawing reveals much useful information regarding the deformation (or orientation) of the filler, strain-induced crystallization, and their crystalline transitions.

Over the last decade, an in-situ small angle X-ray scattering (SAXS) method during tensile stretching of various thermoplastic elastomers has been extensively used to study their deformation behavior [9,10]. SAXS is one of the most advantageous methods to visualize nano-sized fillers such as clay, POSS, cellulosic nanocrystals, graphene, carbon nanotubes, etc. in their nanocomposites [11]. The mechanical properties of the clay nanocomposites have

---

[*] Corresponding author. Tel.: +82 53 950 5630; fax: +82 53 950 6623.
E-mail address: psy@knu.ac.kr (S.-Y. Park).

0032-3861/$ – see front matter © 2012 Elsevier Ltd. All rights reserved.
doi:10.1016/j.polymer.2012.05.037

been reported to be related to the dispersion state of the clay in the polymer matrix. The clay particles can exist as flocculated, intercalated, or exfoliated states in the polymer matrix depending on the processing conditions and the interactions between polymer matrix and clay filler. The dispersion state of clay in a polymer matrix can be analyzed from the gallery gap of the clays through the SAXS peaks [12–14]. B. Finnigan et al. studied the effects of the size of clay disks on the morphologies and the mechanical properties during uniaxial drawing [15]. They found that different size of layered silicates do not have observable effect on the phase separated morphology but decrease in the disk diameter caused a sharp upturn in the stress–strain curve and pronounced increase in tensile strength. The crystal–crystal transitions were also observed during tensile tests and the unique mechanical properties were dependent on the kind of the crystal structure present in the material [16,17]. The deformation-induced phase transitions of some vital polymers such as syndiotactic polypropylene (sPP) [18], polyethylene terephthalate (PET) [19], PA-6 [20,21] and PA-12 [22] have been widely studied. However, there are few studies on the in-situ structural characterizations of the clay (and POSS) nanocomposites during tensile testing in order to study both the change in crystal structure of the polymer matrix and the deformation of the filler during tensile deformation with an in-situ simultaneous SAXS and WAXS experiment.

In this article, we studied nanocomposite systems based on PEBA 6333, which consisted of 60.5 mol % PA-12 as the hard segment and 37.0 mol % PTMO as the soft segment. Tsp-POSS and organically modified clay were used as fillers which are three-dimensional and two-dimensional sheet fillers, respectively. Particularly, the hydroxyl groups in the fillers and amide and ether bonds in the matrix (which can induce hydrogen bonding interactions between the polymer matrix and fillers) may help the nanoscopic dispersion of the fillers in the polymer matrix. Improved mechanical properties were expected from the nanocomposites due to hydrogen bonding interactions of fillers with the PEBA 6333. These well-dispersed nanocomposite systems were analyzed using an in-situ simultaneous SAXS and WAXS technique during uniaxial deformation in order to obtain the step by step structural evolution difference between nanocomposites and PEBA 6333.

2. Experimental

2.1. Materials and nanocomposites preparation

PEBA 6333 was purchased from Arkema©. Cloisite 30B (C30B) was purchased from Southern Clay©. According to the analytical sheet from the supplier, this clay was organically modified with 30 wt% of methyl tallow bis(2-hydroxylethyl) quaternary ammonium salt. Tsp-POSS was purchased from Hybrid Plastics Co., USA. The molecular structures of P6333, the surfactant used to modify the clay, and tsp-POSS are shown in Fig. 1. All the mentioned materials were dried at 120 °C in vacuum for 6 h. The PEBA/organoclay and PEBA/tsp-POSS nanocomposite with a filler content of 2 wt% were prepared by melt mixing in a Haake Rheocorder at 180 °C using a rotor speed of 60 rpm with a mixing time of 10 min, respectively. The nanocomposite materials were hot-pressed at 190 °C and the films were quenched into the icy water. The PEBA/organoclay and PEBA/tsp-POSS nanocomposites are denoted as P6333/C30B and P6333/POSS, respectively.

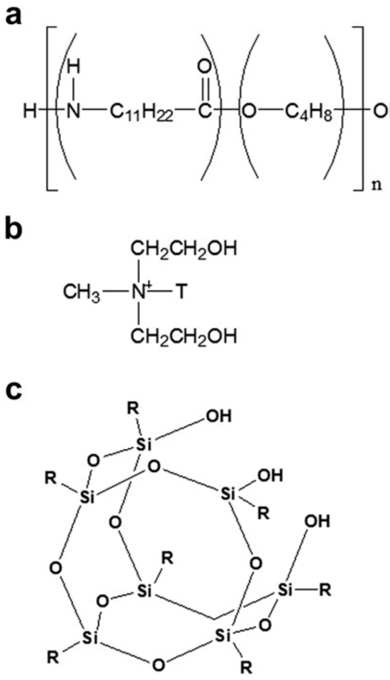

Fig. 1. The chemical structures of (a) P6333, (b) bis(2-hydroxylethyl) quaternary ammonium surfactant used to modify the pristine clay in which T denotes the tallow, and (c) POSS in which R represents the phenyl groups.

2.2. Measurements and data treatment

Fourier transform infrared (FT-IR) spectra of the samples were obtained by a JASCO spectrometer (FT/IR-620). All spectra were recorded in the 4000–400 cm^{-1} range at a 4 cm^{-1} resolution. Pure polymer and nanocomposite films were scratched by a blade to get very thin sections which were later on mixed with KBr to prepare pallets for FT-IR measurements. Differential scanning calorimetry (DSC) measurements were performed on a Setaram instrument (DSC 131 evo) between −80–180 °C. During a typical experiment, an 8 mg sample in a 30 μL aluminium pan was heated at a constant rate of 5 °C/min. The percent crystallinities (X_cs) in the samples were calculated from the melting enthalpy assuming the enthalpy of 100% crystallinity of the γ form of PA-12 as 209.34 J/g [23]. In-situ simultaneous SAXS, WAXS and uniaxial deformation measurements were carried out at the SWAXS beamline BL23A of the National Synchrotron Radiation Research Centre (NSRRC), Taiwan. Strain–stress (S–S) curve, SAXS and WAXS data were simultaneously obtained during uniaxial deformation. With an 10.01 keV (wavelength $\lambda = 1.24$ Å) beam, simultaneous SAXS/WAXS were conducted using two area detectors triggered by the same signals for synchronized data collection. The detector system included a CMOS flat panel X-ray detector C9728DK (52.8 mm square) situated 11.8 cm from the sample position for WAXS and a MAR165 CCD detector (165 mm in diameter), 194.5 cm from the sample position for SAXS [24]. All SAXS and WAXS data were corrected for electronic noise, background scattering and detector sensitivity. The wave vector q ($=4\pi\sin(\theta/2)/\lambda$ where θ is the scattering angle and λ is the wavelength of the X-ray) was calibrated with a standard sample of silver behenate. A Linkam TST-350 (Tensile Stress Testing System) was used for the uniform uniaxial stretching of the samples. The tensile tester was controlled via PC through Linksys 32× system control software which displays and saves online plots of temperature, force, and distance. For tensile testing, dog-bone-shaped sample bars with dimensions of 18.0 mm (length) × 4.0 mm (neck width) × 0.6 mm (thickness) were prepared after compression molding at 190 °C. A constant uniaxial stretching rate of 2 mm/min was applied to the specimen throughout the deformation study at 25 °C. The yielding strain (ε_y) and the strain starting strain- hardening (ε_h) on the S–S curve were determined from a cross-section point of the two tangent lines at the strains in the initial elastic and plateau regions and in the plateau and strain-hardening regions, respectively. The WAXS detector was mounted such that the major 001 reflection of the γ form of PA-12 (001_γ) could be located in the detector at high strains. The two dimensional (2D) patterns were scanned with the FIT2D software package to obtain the one dimensional (1D) patterns in the form of intensity vs. q. The long period in region I was calculated from Bragg equation of $d = 2\pi/q_{max}$ where q_{max} corresponds to the peak position calculated with the Gaussian peak fitting method from the 1D patterns using the Origin 7.0 software.

3. Results and discussion

3.1. Interactions between the fillers and the polymer matrix

The interactions between the dispersed fillers and the polymer matrix were studied by using the FT-IR spectroscopy. Fig. 2 shows the FT-IR spectra of P6333, P6333/POSS, and P6333/C30B in the hydrogen bonding (H-bonding) regions. In Fig. 2a, P6333 has a peak at 1638 cm^{-1} which corresponds to the C=O stretching vibration of amide I. This peak was shifted to the lower positions of 1635 and 1634 cm^{-1} in the FT-IR spectra of P6333/C30B, and P6333/POSS, respectively. This shifting might be due to the H-bonding between the amide groups of P6333 and the hydroxyl (OH) groups in the POSS and the C30B [6]. Fig. 2b shows an ether (C-O-) band of P6333 at 1112 cm^{-1} which was shifted to the lower positions of 1103 and 1108 cm^{-1} for P6333/C30B and P6333/POSS, respectively, due to the H-bonding between the ether groups in PTMO and the OH groups in the C30B and POSS. It should be noted that these hydrogen bonds affecting the FT-IR peak position were attributed to the functional groups in the amorphous region since the fillers could exist only in the amorphous region.

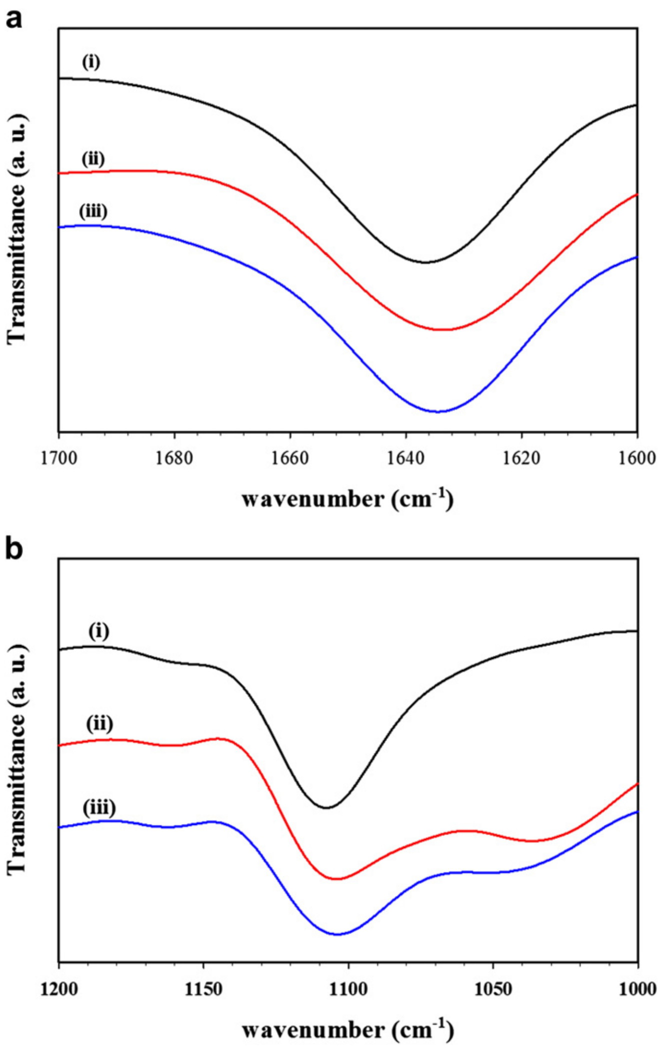

Fig. 2. FT-IR spectra of (i) P6333, (ii) P6333/C30B, and (iii) P6333/POSS in the ranges of (a) 1600–1700 cm^{-1} for the amide I band, and (b) 1000–1200 cm^{-1} for the ether band.

The thermal properties of P6333, P6333/POSS, and P6333/C30B were analyzed with DSC and the thermograms are shown in Fig. 3. P6333 showed a single glass transition temperature (T_g) at 51.1 °C due to the PA-12 block [23]. The T_g of the PTMO block was not observed due to its small amount in P6333 compared to other PEBA grades such as P2533 and P4033 which have more PTMO contents in the copolymer [1]. The crystallinities, the melting temperatures (T_ms) and the T_gs are presented in Table 1. The T_gs of P6333/POSS, and P6333/C30B slightly increased compared to P6333 due to the H-bonding between polymer matrix in amorphous region and the functional groups in the fillers. The T_ms and the crystallinities of P6333/POSS and P6333/C30B were 169.7 °C and 54% and 170.1 °C and 60%, respectively, which a little increased from that of P6333 (169.6 °C and 42%). An increase in the crystallinity and the T_m in the nanocomposites compared to P6333 can be understood from the enhanced nucleation effect of the foreign materials as reported for other semi-crystalline polymers such as PA-6 and PA-66 [25,26].

3.2. Classification of the deformation regions

Fig. 4 shows the S–S curves of P6333, P6333/POSS, and P6333/C30B at room temperature during the in-situ experiments. Sheth et al. [1] placed the P6333 in the thermoplastic category rather than an elastomer since they observed a clear yield point in the S–S curve. We observed the yielding at strains (ε_ys) = 15, 10, and 9% for P6333, P6333/POSS, and P6333/C30B, respectively, shown by the arrows in Fig. 4. Young's moduli and breaking strengths of P6333/POSS and P6333/C30B were, respectively, 547 and 69.8 MPa and 666 and 58.0 MPa, while that of P6333 were 234 and 49.0 MPa. Elongations at break of P6333/POSS and P6333/C30B were 322 and 218%, respectively, compared to 412% of P6333. The increases in strength (and modulus) and the decreases in elongation at breaking point of the nanocomposites were due to a reinforcing effects of the

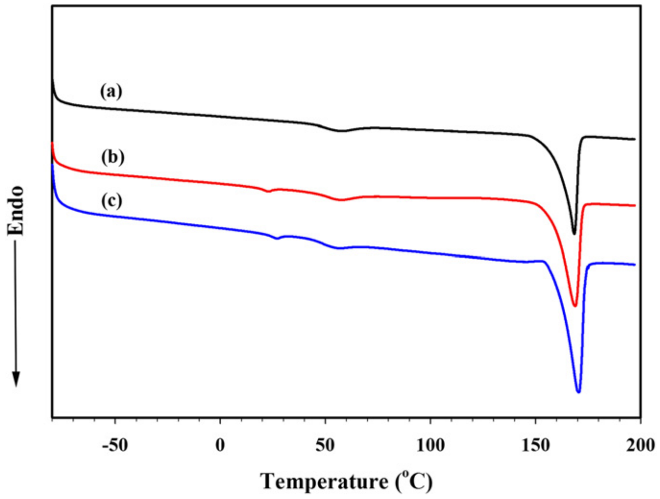

Fig. 3. DSC thermograms of (a) P6333, (b) P6333/POSS, and (c) P6333/C30B.

Table 1
Parameters calculated from the DSC thermograms in Fig. 1.

Sample	Glass transition temperature (°C)	Melting temperature (°C)	Crystallinity (%)
P6333	51.7	169.6	42
P6333/POSS	54.7	169.7	54
P6333/C30B	53.8	170.1	60

added fillers as commonly observed in other composite systems [27]. After yielding, the stress was nearly constant up to a certain strain (ε_h) after which the stress started to increase again due to strain-hardening effect [28]. The ε_hs were 100, 84, and 80% for P6333, P6333/POSS, and P6333/C30B, respectively. Each S–S curve could be divided into three regions; the elastic deformation before yielding (region I, 0 to ε_y), the plateau (region II, ε_y to ε_h), and the strain-hardening (region III, after ε_h) regions. These regions could be identified from the arrows on the S–S curves. The structural changes in each region of the S–S curve were studied with the in-situ simultaneous WAXS and SAXS methods during uniaxial drawing at next section.

3.3. *Structural evolution during tensile drawing*

The 2D WAXS and SAXS patterns of P6333, P6333/POSS, and P6333/C30B at different εs are shown in Fig. 5. The 2D WAXS patterns of P6333, P6333/POSS, and P6333/C30B at $\varepsilon = 0\%$ (undrawn state) had three isotropic crystalline reflections indexed as 020, 040, and 001 of the stable γ form of the PA-12. These reflections became clearer as the ε increased. The 001 reflection was located on the equator and the 020 and 040 reflections were positioned on the meridian in the elongated state. The γ form of PA-12 is one of the most commonly observed crystal phases with a pseudo-hexagonal packing. This γ form is monoclinic with a space group of $P2_1/c$ and lattice parameters of $a = 4.79$ Å, $b = 31.9$ Å (fiber axis), $c = 9.58$ Å, and $\beta = 120°$ in which there are four monomeric units [29]. The long alkyl group of the PA-12 monomer in the crystal is in a planar zigzag conformation except at the position of the amide groups which are twisted. H-bonds are formed between the neighboring chains, leading to the formation of the parallel sheet structure that is a distinct feature of the γ form. The 2D SAXS patterns of P6333, P6333/C30B, and P6333/POSS at $\varepsilon = 0$ had a diffused isotropic ring at $q = \sim 0.4$ nm^{-1}. This diffused isotropic ring was thought to be due to the microphase-separated PA-12 crystalline lamellae between the mixed amorphous PTMO and PA-12 phases. At vicinity of the beam stopper, strong scattering was observed for P6333/POSS and P6333/C30B nanocomposites due to the high electron density of the silicon and aluminum in the fillers. In contrast to P6333 and P6333/POSS, the lamellar peak of P6333/C30B was not clear due to the strong scattering from clay and less development of the lamellar structure, therefore, we could not discuss its lamellar structure and crystalline orientation. Fig. 6 shows the azimuthally averaged 1D data from the 2D WAXS patterns between $-15°$ and $15°$ along equatorial and meridional directions as functions of q and ε for P6333, P6333/POSS, and P6333/C30B with $\Delta\varepsilon = 14\%$ between two adjacent curves. The data along the equator was in the range of $q = 10$–20 nm^{-1} which covers the 001_γ reflection and that along the meridian was in the range of $q = 2$–6 nm^{-1} which covers the 020 reflection. At $\varepsilon = 0\%$ along the equator, all scanned data showed the strong 001_γ reflection at $q = 15.21$ nm^{-1} and the weak 002 reflection of the α form at $q = 15.8$ nm^{-1} although its weak intensity indicated that the amount of the α form were small compared to the γ form. In the case of the P6333/C30B, another weak reflection at $q = 14$ nm^{-1} was detected. This reflection was due to the reflection of the clay sheet. At $\varepsilon = 0\%$ along the meridian, the 020 reflection at $q = \sim 4.23$ nm^{-1} was observed for all samples although two additional reflections at $q = 5.2$ and 5.7 nm^{-1} [30] for P6333/POSS were due to the presence of the POSS.

In region I, there was no considerable change in the WAXS patterns of the P6333, P6333/POSS, and P6333/C30B (in terms of the PA-12 crystal orientation and the crystalline peak position) as the ε increased. However, the SAXS patterns became anisotropic so that the scattering maximum started shifting towards a low angle along the meridian while the scattering along the equator gradually disappeared without changing position so that the patterns became oblate. The decrease of the scattering maximum along the stretching direction was due to the increase in the inter-lamellar distance while the decrease in intensity along the transverse direction indicated that the amounts of the lamellae oriented along the transverse direction decreased. The d-spacing of the 001_γ reflection (d_{001}) slightly decreased from $d = 0.410$ to 0.407 nm for all samples (Fig. 6d). In this initial region, the elastic deformation mostly occurred between the chain entanglements in the amorphous region so that the positions of the 001 and 020 reflections had little change.

In region II, the meridional scatterings in the SAXS patterns of P6333 and P6333/POSS started to split into four points. This four-point pattern was clear at the end of this region. Appearance of the four-point SAXS pattern suggests that the lamellar structure was fragmentized into small pieces and those fragmented lamellae were tilted against the drawing direction and/or had a checkerboard arrangement to minimize the stress concentration at the lamellae. In the WAXS patterns, the initial strong 001_γ reflection of P6333 became broad with decreased intensity and seemed slightly oriented at the end of region II. The 001_γ reflections of the P6333/POSS and P6333/C30B were more anisotropic and broad than that of the P6333. The d_{001} was nearly constant at $d = 0.407$ nm and that of the 020 reflection (d_{020}) decreased from 1.53 to 1.50 nm with reduced intensity in region II. In this region, disentanglement of the chains in the amorphous region happened so that flow deformation occurred without an increase in stress in the S–S curve. During the flow of the chains, the lamellar structure was fragmentized into the small pieces as discussed before. Besides the four different crystalline forms of the PA-12, Liangbin Li et al. reported a new crystalline form, the α'' phase, which was considered as the transient phase between the room temperature γ- and the final mesomorphic phases during the tensile drawing (the mesomorphic phase will be discussed in the next paragraph) [22]. They also reported

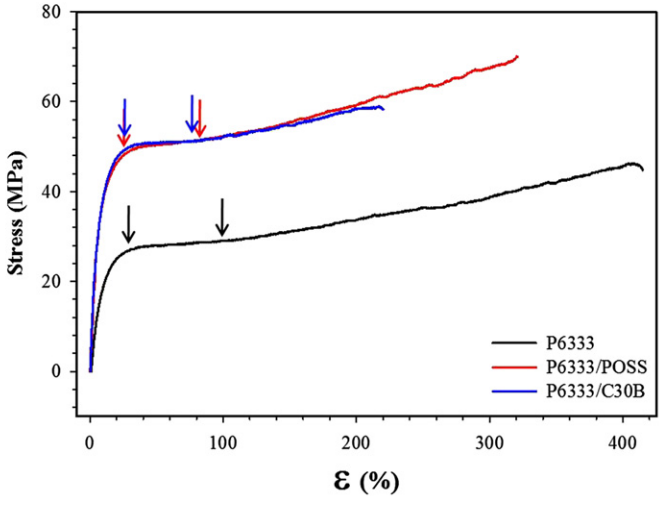

Fig. 4. The S–S curves of P6333, P6333/POSS, and P6333/C30B films.

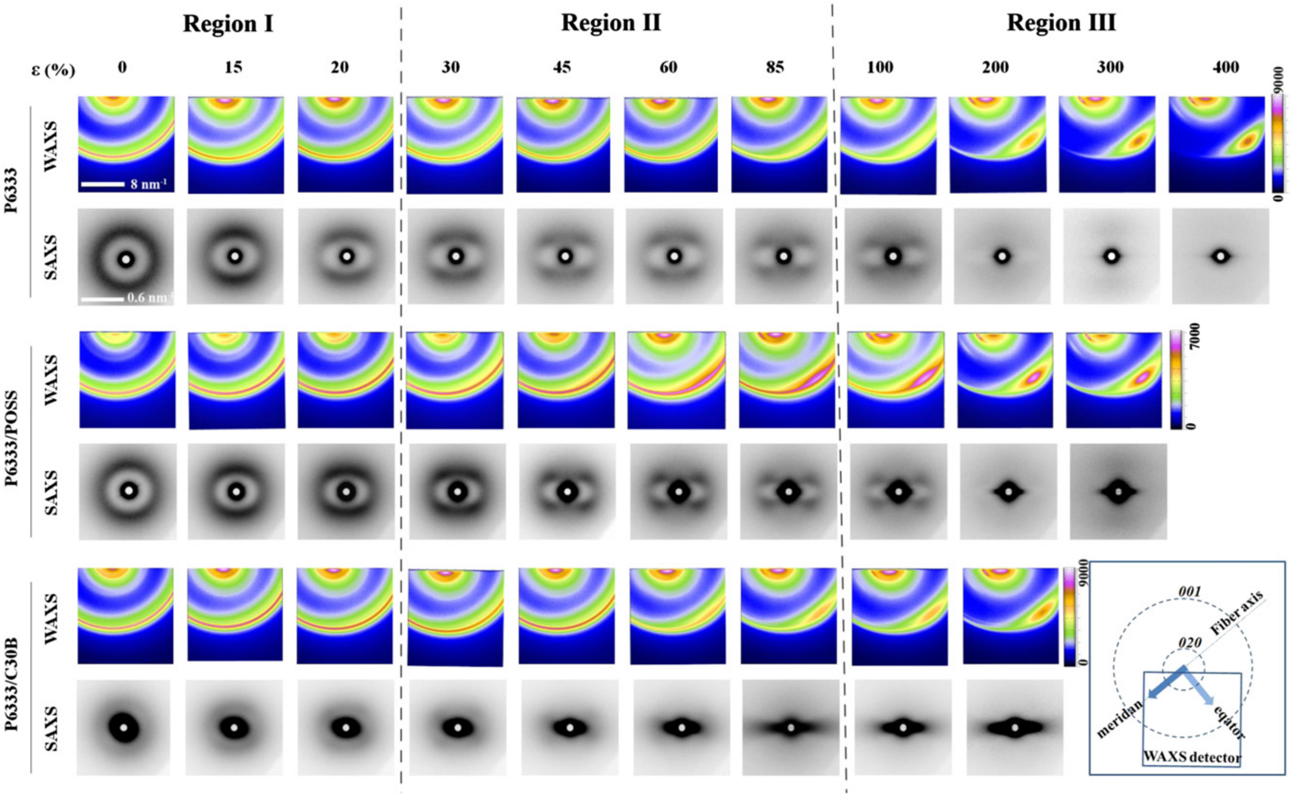

Fig. 5. Selected 2D WAXS and SAXS patterns of P6333, P6333/POSS, and P6333/C30B at different εs; the inset in the right bottom corner shows the orientation of the WAXS detector and the fiber axis for SAXS patterns is vertical. The division of this figure into regions is based on P6333. The scale bars on WAXS and SAXS patterns represent 8 nm^{-1} and 0.6 nm^{-1}, respectively.

that the α'' phase is more prominent and lives longer life in elastomers compare to PA-12 homopolymer. This α'' phase might exist in this region although it needs more clarification due to the weak intensities of the reflections from the α'' phase.

In region III, the broadness of the oriented 001 reflection was obvious and the 020 reflection became more anisotropic for all three samples in the WAXS patterns. In the SAXS patterns, the positions of the scattering maxima of the four-point patterns did not change although their intensities decreased upon further increase in ε. At the expense of the decrease in their intensity, a new meridional peak appeared at $\varepsilon = 300\%$ for P6333 and P6333/POSS. Neither the intensity nor the position of this peak changed with further elongation until the failure of the sample. Stress was built up again in this region of the S–S curve. Cases have been reported for elastomers containing higher soft segments in the samples where the building up of stress in the last region of the S–S curve was regarded to the soft segment's strain-induced crystallization [31,32]. However, we could not find any reflections from the PTMO crystal. It is reported that the γ crystal structure of the PA-12 changed to the mesomorphic structure in this strain-hardening region during mechanical drawing. The sharpness of the 001 reflection in regions I and II vanished and was replaced with a broad one. This broad peak around the 001 reflection was reportedly due to the mesomorphic crystal structure of the PA-12 [22]. The mesomorphic structure was produced because most of the polymer chains in the amorphous part of the sample became fully aligned along the stretching direction from their initial relaxed state at the end of region II and further elongation at region III transferred the stretching force to the PA-12 crystal causing the γ to mesomorphic crystal structure transition. The newly formed mesomorphic structure might be responsible for the new meridional scattering in the SAXS pattern. This mesomorphic structure lost their three dimensional ordering because the hydrogen bonding positions in the crystal was mismatched by mechanical drawing. The d_{020} of P6333 increased again due to the elongation of the alkyl chain in the crystal by increased applied stress due to strain-hardening. The d-spacing of the peak around the 001 reflection due to mesomorphic structure (d_m) increased and was saturated at $d = 0.423$ nm. This increase might be due to the dilation between adjacent chains through the loss of the compact packing order in the mesomorphic structure.

3.4. Deformation of the composites

For the nanocomposite cases, similar trends were observed with the pure one except the ε_h values of regions I, II and III and for the appearance of the filler scatterings. The strong interactions between the fillers and matrix caused the strain-hardening at a smaller ε_hs than that of the pure polymer and caused the direct transfer of the force to the PA-12 crystals rather than dissipating in the amorphous region, therefore, the increase in the d_m due to the mesomorphic structure occurred at small εs for P6333/POSS and P6333/C30B compared to P6333. In the case of P6333/C30B SAXS patterns, the clay scattering adopted an ellipsoidal shape with their long axis perpendicular to the draw direction. This result indicates that the surface of the clay was oriented more parallel to the film

Fig. 6. The azimuthally averaged 1D data from the 2D WAXS patterns between −15° and 15° along equatorial (a, b, c) and meridional (e, f, g) directions as functions of q and ε for (a, e) P6333, (b, f) P6333/POSS, and (c, g) P6333/C30B with $\Delta\varepsilon = 14\%$ between two adjacent curves; (d) and (h) are the d-spacings at the maximum intensity of (a, b, c) and (e, f, g) as a function of ε, respectively. The division of (d) and (h) into regions is based on P6333.

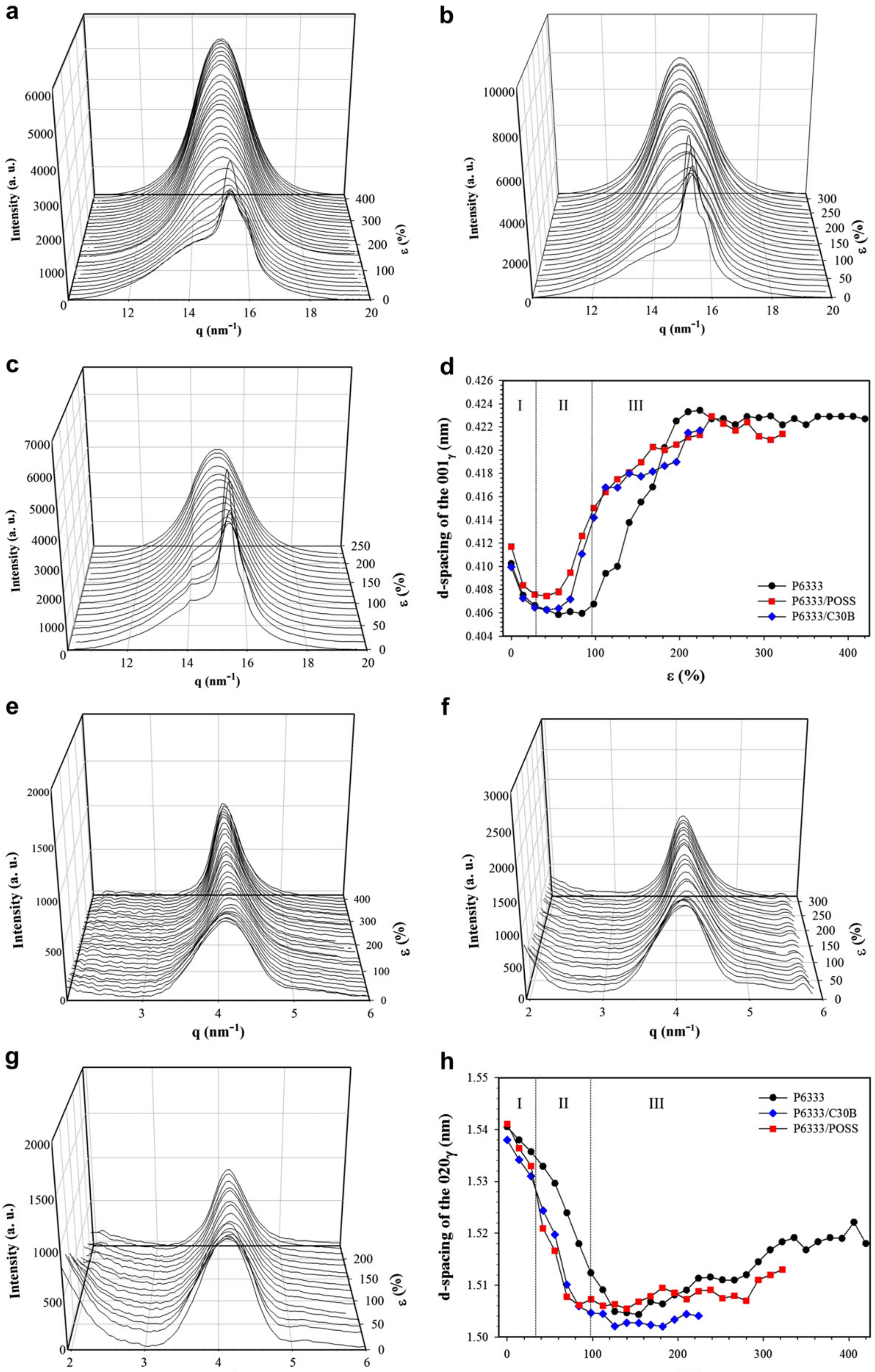
a
Intensity (a. u.)
q (nm^{-1})
ε (%)
b
Intensity (a. u.)
q (nm^{-1})
ε (%)
c
Intensity (a. u.)
q (nm^{-1})
ε (%)
d
d-spacing of the 001$_\gamma$ (nm)
ε (%)
I
II
III
P6333
P6333/POSS
P6333/C30B
e
Intensity (a. u.)
q (nm^{-1})
ε (%)
f
Intensity (a. u.)
q (nm^{-1})
ε (%)
g
Intensity (a. u.)
q (nm^{-1})
ε (%)
h
d-spacing of the 020$_\gamma$ (nm)
ε (%)
I
II
III
P6333
P6333/C30B
P6333/POSS

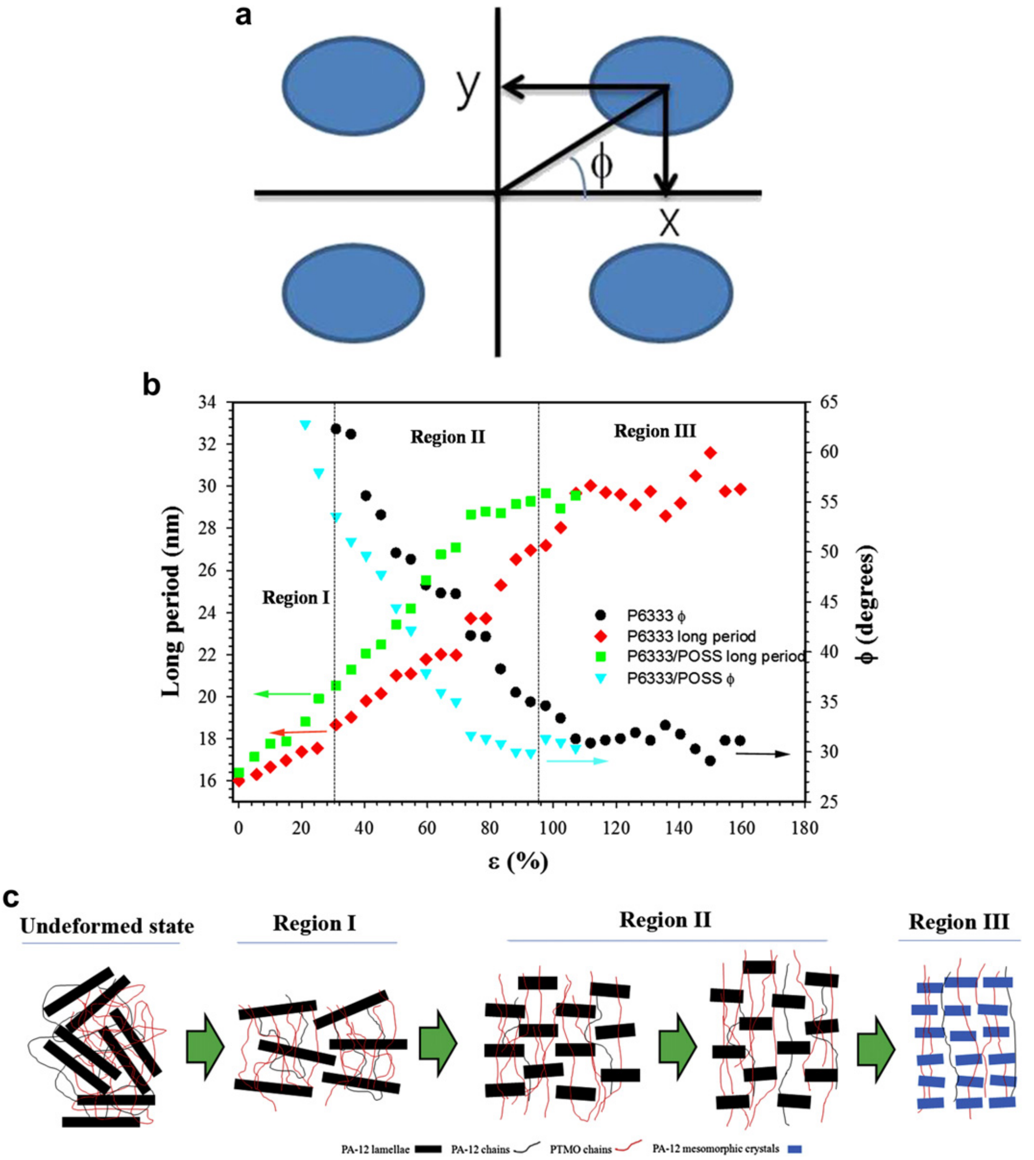

Fig. 7. (a) The Cartesian x and y coordinates of the four points with the definition of the ϕ, (b) the long periods and the ϕs of P6333, and P6333/POSS as functions of ε, (c) the pictorial representation of the lamellar structures in regions I, II, and III.

surface as the ε increased. Similar results were reported by us for the PA-6/clay nanocomposites [33]. The POSS nanocomposites with different polymer matrices have been studied in the past. It has been well established that their molecules lie in the form of crystalline aggregates of various sizes. In the case of the SAXS patterns of P6333/POSS, the scattering around the beam stopper was an isotropic spherical shape at all εs contrary to P6333/C30B, which changed from the isotropic shape to the anisotropic one as the ε increased. A streak also appeared oriented along the equator at $\varepsilon \geq 100\%$ and became apparent and elongated at higher εs. The appearance of the streak occurred at smaller ε of 100% in P6333/POSS compare to pure P6333 where it occurred at ∼200% (see Fig. 5). The spherical shape around the beam stopper and the appearance of the streak might be due to reflecting the spherical shape of POSS and the microvoid formation, respectively, which would have weakened the sample and made it unable to withstand with high stretching force. Thus, the elongation at the breaking point of P6333/POSS was less than that of the neat polymer.

3.5. *Lamellar deformation*

The initial isotropic SAXS patterns became oblate in region I and four-point in the regions II and III although the new meridional scattering due to the mesomorphic structure overlapped in region III as discussed above (see Fig. 5). As the ε increased, the lamellar structure was fragmentized into a checkerboard arrangement as previously mentioned. This fragmentation with checkerboard arrangement caused the four-point pattern. In the checkerboard arrangement, the distance between the lamellae (long period) can be analyzed by the layer distance of the four points pattern (y value in the Cartesian x and y coordinates where x and y represents the horizontal and vertical values of the four points as shown in Fig. 7a). The long period can be defined as $2\pi/y$. The amounts of the staggering between lamellae can be analyzed by the angle between a separated maximum point in the four-point pattern and the horizontal direction (ϕ, no staggering happens when $\phi = 90°$) shown in Fig. 7. In region I where the four-point pattern was not observed, the d-spacing of the scattering along the meridian is long period because only the oblate pattern was observed as discussed in Fig. 5. Fig. 7b shows the long periods and the ϕs of P6333, and P6333/POSS as a function of ε. We could not analyze P6333/C30B because of the weak intensity as discussed above. The initial long period increased slowly from 16 to 18 nm in region I for both the pure P6333 and P6333/POSS. Further determination of long period from the layer distance analysis of the four-points pattern suggests that the process of increase in long period continued in region II which saturated in region III. The ε at which the long period was saturated was the same as the ε_h. The increase of the long period mostly happened due to elongation of the flexible amorphous chains between the lamellae. This increase of the long period could not occur further since the amorphous chains were fully elongated in region III. Further stretching might cause the plastic deformation of the film and the stretching force could be transferred more efficiently to the crystal; thereby, a transition of the distinct γ crystal to the mesomorphic structure resulting in new lamellar structure formation could occur.

Based on the results from the SAXS data, the models for the deformation of the PA-12 crystalline lamellae were proposed in Fig. 7c. The isotropic SAXS pattern in the undeformed state shows the PA-12 crystalline lamellae with random orientation. In region I, the increased intensity with slight change of the intensity maximum towards smaller angles on the meridian in the SAXS patterns suggests that the lamellae had increased inter-lamellar distance with slight orientation along the drawing direction. In region II, four-point patterns appeared and their location changed upon further elongation as explained in Fig. 7b. This suggests that the lamellae were fragmented into a checkerboard arrangement in which the inter-lamellar distance and the angle between the normal of the reflection plane and the drawing direction (ϕ) increased as the ε increased due to elongation of the amorphous part. In region III, a new meridional peak in the SAXS pattern appeared at higher angles than those of the four-point pattern with disappearance of the four-point pattern. This observation indicated that the existing crystals were melted down and simultaneously new mesomorphic crystals (blue ones) appeared with shorter inter-lamellar distance.

4. Conclusions

The structures of P6333, P6333/C30B, and P6333/POSS were explored for model studies on poly(ether-b-amide) nanocomposite systems with two- and three-dimensional nano-sized fillers of the organically modified clay and POSS, respectively. These fillers had H-bonding capability with the P6333 matrix which caused their better dispersion, the improved mechanical properties and the increased T_g in the nanocomposites compared to the pure P6333. The crystallinity also increased due to the role of the fillers as nucleating agents. During the uniaxial deformation of the samples, the three regions based on the slopes in the S-S curves could be divided. In region I, the elastic deformation happened mostly in the amorphous region and the crystal structure was the γ form of the PA-12. In region II, the lamellae were fragmentized and their checkerboard arrangements occurred giving a four-point SAXS pattern by flow deformation although the WAXS patterns hardly changed in terms of the crystal orientation and the peak position. In region III, the elongation of chains in the amorphous region between lamellae reached maximum so that the further stretching caused the strain-hardening and its force was directly transferred to the crystal leading to the transition of the γ crystal to the mesomorphic structure. The profound difference in the P6333/C30B and P6333/POSS compared to the pure P6333 was the appearance of regions II and III occurring at a low ε because the strong interactions between fillers and matrix. The surface of the clay in the P6333/C30B was oriented more parallel to the film surface with an increase in ε and microvoids were detected in the P6333/POSS.

Acknowledgments

This research was supported by the Fundamental R&D Program for Core Technology of Materials funded by the Ministry of Knowledge Economy, Republic of Korea and the national research foundation of Korea (NRF) grant funded by Korea government (MEST) (No. 2011-0020264). Synchrotron work was supported in part by the Ministry of Science & Technology (MOST), by POSCO, by the Center for Integrated Molecular System (Korea Science & Engineering Foundation), and by the KISTEP (Basic Research Grant of Nuclear Energy, MOST).

References

[1] Sheth JP, Xu JN, Wilkes GL. Polymer 2003;44(3):743–56.
[2] Shin J, Matsushima H, Chan JW, Hoyle CE. Macromolecules 2009;42(9):3294–301.
[3] Waletzko RS, Korley LTJ, Pate BD, Thomas EL, Hammond PT. Macromolecules 2009;42(6):2041–53.
[4] www.pebax.com.
[5] Feller JF, Langevin D, Marais S. Synthetic Metals 2004;144(1):81–8.
[6] Le NL, Wang Y, Chung TS. Journal of Membrane Science 2011;379(1–2):174–83.
[7] Bourbigot S, Duquesne S, Jama C. Macromolecular Symposia 2006;233:180–90.
[8] Atanasoska LE, Weber Jan, Warner Robert. Polymeric/Inorganic composite materials for Use in Medical Devices. United states. Maple Grove, MN, US: BOSTON SCIENTIFIC SCIMED, INC.; 2010.
[9] Liu LZ, Hsiao BS, Fu BX, Ran SF, Toki S, Chu B, et al. Macromolecules 2003;36(6):1920–9.
[10] Pereira IM, Orefice RL. Polymer 2010;51(8):1744–51.
[11] Ray SS, Okamoto M. Progress in Polymer Science 2003;28(11):1539–641.
[12] Sun DW, Li YF, Zhang B, Pan XB. Composites Science and Technology 2010;70(6):981–8.
[13] Alexandre B, Langevin D, Mederic P, Aubry T, Couderc H, Nguyen QT, et al. Journal of Membrane Science 2009;328(1–2):186–204.
[14] Tolle TB, Anderson DP. Composites Science and Technology 2002;62(7–8):1033–41.
[15] Finnigan B, Jack K, Campbell K, Halley P, Truss R, Casey P, et al. Macromolecules 2005;38(17):7386–96.
[16] Liu Y, Cui L, Guan FX, Gao Y, Hedin NE, Zhu L, et al. Macromolecules 2007;40(17):6283–90.
[17] De Rosa C, Auriemma F. Angewandte Chemie International Edition 2012;51(5):1207–11.
[18] Auriemma F, De Rosa C, Esposito S, Mitchell G. Angewandte Chemie International Edition 2007;46(23):4325–8.
[19] Welsh GE, Blundell DJ, Windle AH. Journal of Materials Science 2000;35(20):5225–40.
[20] Penel-Pierron L, Seguela R, Lefebvre JM, Miri V, Depecker C, Jutigny M, et al. Journal of Polymer Science Part B-Polymer Physics 2001;39(11):1224–36.
[21] Miri V, Persyn O, Lefebvre JM, Seguela R, Stroeks A. Polymer 2007;48(17):5080–7.
[22] Wang DL, Shao CG, Zhao BJ, Bai LG, Wang X, Yan TZ, et al. Macromolecules 2010;43(5):2406–12.
[23] Sandler JKW, Pegel S, Cadek M, Gojny F, van Es M, Lohmar J, et al. Polymer 2004;45(6):2001–15.
[24] Wu WR, Jeng US, Su CJ, Wei KH, Su MS, Chiu MY, et al. ACS Nano 2011;5(8):6233–43.
[25] Fornes TD, Paul DR. Polymer 2003;44(14):3945–61.
[26] Liu XH, Wu QJ, Berglund LA. Polymer 2002;43(18):4967–72.
[27] Hakimelahi HR, Hu L, Rupp BB, Coleman MR. Polymer 2010;51(12):2494–502.
[28] Zhang XQ, Schneider K, Liu GM, Chen JH, Bruning K, Wang DJ, et al. Polymer 2011;52(18):4141–9.
[29] Hoshino KIaS. Journal of Polymer Science: Polymer Physics Edition 1973;11:1077–89.
[30] Wan CY, Zhao F, Bao XJ, Kandasuramanian B, Duggan M. Journal of Polymer Science Part B-Polymer Physics 2009;47(2):121–9.
[31] Koerner H, Kelley JJ, Vaia RA. Macromolecules 2008;41(13):4709–16.
[32] Khan U, Blighe FM, Coleman JN. Journal of Physical Chemistry C 2010;114(26):11401–8.
[33] Park SY, Cho YH, Vaia RA. Macromolecules 2005;38(5):1729–35.